Establishing accretion flares from massive black holes as a major source of high-energy neutrinos

S. van Velzen[1], R. Stein[2, 3, 4], M. Gilfanov[5, 6], M. Kowalski[2,3], K. Hayasaki[7, 8], S. Reusch[2,3], Y. Yao[9], S. Garrappa[2,3], A. Franckowiak[2,10], S. Gezari[11,12], J. Nordin[3], C. Fremling[4], Y. Sharma[9], L. Yan[13], E. C. Kool[14], J. Sollerman[14], P. Medvedev[5], R. Sunyaev[5,6], E. Bellm[15], R. G. Dekany[13], D. A. Duev[4], M. J. Graham[4], M. M. Kasliwal[4], R. R. Laher[16], R. L. Riddle[13], and B. Rusholme[16]

[1]*Leiden Observatory, Leiden University, Postbus 9513, 2300 RA, Leiden, The Netherlands*
[2]*Deutsches Elektronen Synchrotron DESY, Platanenallee 6, D-15738 Zeuthen, Germany*
[3]*Institut für Physik, Humboldt-Universität zu Berlin, D-12489 Berlin, Germany*
[4]*Division of Physics, Mathematics, and Astronomy, California Institute of Technology, Pasadena, CA 91125, USA*
[5]*Space Research Institute, Russian Academy of Sciences, Profsoyuznaya ul. 84/32, Moscow, 117997, Russia*
[6]*Max-Planck-Institut für Astrophysik, Karl-Schwarzschild-Str. 1, D-85741 Garching, Germany*
[7]*Department of Astronomy and Space Science, Chungbuk National University, Cheongju 361-763, Republic of Korea*
[8]*Harvard-Smithsonian Center for Astrophysics, 60 Garden Street, Cambridge, MA02138, USA*
[9]*Cahill Center for Astrophysics, California Institute of Technology, MC 249-17, 1200 E California Boulevard, Pasadena, CA 91125*
[10]*Fakultät für Physik & Astronomie, Ruhr-Universität Bochum, D-44780 Bochum, Germany*
[11]*Space Telescope Science Institute, 3700 San Martin Dr., Baltimore, MD 21218, USA*
[12]*Department of Astronomy, University of Maryland, College Park, MD 20742, USA*
[13]*Caltech Optical Observatories, California Institute of Technology, Pasadena, CA 91125, USA*
[14]*The Oskar Klein Centre, Department of Astronomy, Stockholm University, AlbaNova, SE-10691, Stockholm, Sweden*
[15]*DIRAC Institute, Department of Astronomy, University of Washington, 3910 15th Avenue NE, Seattle, WA 98195, USA*
[16]*IPAC, California Institute of Technology, 1200 E. California Blvd, Pasadena, CA 91125, USA*

November 19, 2021

High-energy neutrinos have thus far been observed in coincidence with time-variable emission from three different accreting black holes: a gamma-ray flare from a blazar (TXS 0506+056), an optical transient following a stellar tidal disruption (AT2019dsg), and an optical outburst from an active galactic nucleus (AT2019fdr). Here we present a unified explanation for the latter two of these sources: accretion flares that reach the Eddington limit. A signature of these events is a luminous infrared reverberation signal from circumnuclear dust that is heated by the flare. Using this property we construct a sample of similar sources, revealing a third event coincident with a PeV-scale neutrino. This sample of three accretion flares is correlated with high-energy neutrinos at a significance of 3.7σ. Super-Eddington accretion could explain the high particle acceleration efficiency of this new population.

Accreting black holes have long been suggested as potential sources of high-energy particles (*1, 2*) and this expectation was supported by the detection of a high-energy neutrino coincident (at the 3σ-level) with gamma-ray flaring from the blazar TXS 0506+056 (*3*). However, blazars alone cannot account for the observed high-energy neutrino flux (*4, 5*); similar to the electromagnetic sky, we can expect that the observed cosmic neutrino flux (*6*) arises from multiple source populations (*7*).

In the last two years, optical follow-up observations of neutrino alerts (*8*) using the Zwicky Transient Facility (ZTF, (*9*)) have identified two optical flares from the centers of galaxies coincident with PeV-scale neutrinos: AT2019dsg (*10*) and AT2019fdr (*11*). The former belongs to the class of spectroscopically-classified tidal disruption events (TDEs) from quiescent black holes, while the latter originated from a type 1 (i.e., unobscured) active galactic nucleus (AGN). However, the distinctive shared properties we present below suggest these flares share a common origin.

Both events show a large amplitude optical flare with a rapid rise time, signalling a sudden increase of the mass accretion rate onto the supermassive black hole. Of the $\sim 10^4$ AGN detected by ZTF (*12*), less than 1% show similarly rapid and large outbursts (*11*).

The most important unifying signature of the two neutrino-coincident ZTF sources is delayed transient infrared emission, detected by NEOWISE (*13*). This infrared emission is due to reprocessing of the optical to X-ray output of the flare by hot dust ($T \sim 2 \times 10^3$ K) at distances of 0.1-1 pc from the black hole (*14*). Because the dust reverberation signal is agnostic to the origin of the flare, infrared observations allow us to construct a sample that unifies extreme nuclear flares like AT2019fdr and AT2019dsg. Below we discuss this unified population and present the significance of their correlation with high-energy neutrinos.

Based on the properties of the ZTF light curves (rise time, fade time and amplitude; see Supplement), we define a sample of 1732 *accretion flares*, nuclear transients that are similar to AT2019dsg and AT2019fdr. We search for a significant infrared flux increase after the peak of the optical flare using NEOWISE observations. The NEOWISE light curves cover the period from 2014 to 2020 with a typical accuracy of 20 μJy, providing a sensitive measurement of past activity in the galaxy center. We define the *strength* of the dust echo to be $\Delta F/F_{\rm rms}$: the mean IR flux increase in the first year after the optical transient over the root-mean-square (rms) variability prior to the optical peak. After applying the requirement that the dust echo strength is larger than the significance of the pre-flare variability ($\Delta F/F_{\rm rms} > F_{\rm rms}/\sigma_F$, with σ_F the measurement uncertainty of the baseline flux), we are left with 63 accretion flares that have potential dust echoes.

Black hole mass estimates based on spectroscopy are available for about 1/3 of the accretion flares. We find that strong dust echoes ($\Delta F/F_{\rm rms} > 10$) are observed almost exclusively for events with $M_{\rm BH} < 10^8\,M_\odot$, see Fig. 1. This threshold for strong echoes coincides with the maximum mass for a visible disruption from a solar-type star, motivating the construction of

a *TDE candidate* sample: all accretion flares with $M_{\rm BH} < 10^8\,M_\odot$. The IR properties of the accretion flares with black hole mass estimates are used to place all nuclear transients with dust echoes into a two-tier classification scheme: (1) accretion flares with strong dust echoes and (2) regular AGN variability. Using the public list IceCube neutrino alerts (*8*), we wish to test the hypothesis that the former class is a source of high-energy neutrinos.

To assess the significance of a neutrino and transient association we perform a likelihood ratio test using our signal hypothesis S (that neutrinos are produced by accretion flares with large dust echoes), and our background hypothesis B (that neutrinos are not correlated with accretion flares). For the ith neutrino, we define a Test Statistic (TS) as:

$$\mathrm{TS}_i = 2\log\left[\left(\hat{S}/B\right)_{\rm IC}\left(\hat{S}/B\right)_{\rm area}\left(\hat{S}/B\right)_{\rm echo}\left(\hat{S}/B\right)_{\rm flux}\right] \tag{1}$$

When multiple flares match to a single neutrino, we pick the flare with highest TS ($\hat{S}$) as our best-fit signal hypothesis. If there are no coincident candidates, or the best fit signal TS is smaller than zero, we instead select the null hypothesis as the best fit ($\mathrm{TS}_i = 1$). The first term of Eq. 1 is the "signalness", which measures the probability that a detector track recovered by IceCube is from a cosmic neutrino, based on the reconstructed energy. Next, the area term accounts for the difference in the 90% confidence level (CL) sky area of the reconstructed neutrino position ($\Omega_{\rm IC}$): $(S/B)_{\rm area} = (0.9/\Omega_{\rm IC})\,n_{\rm ran}$. Here $n_{\rm ran} = 0.001$ deg^{-2} is the areal density of random coincidences. The third term of Eq. 1, $(S/B)_{\rm echo}$, is the odds ratio that a flare belongs to the class of dust echoes versus regular variability from AGN, as measured using our training sample of TDE candidates. The final term of Eq. 1, $(S/B)_{\rm flux}$, encodes our expectation for the neutrino flux produced by the transient. We obtain a probability density function for the expected IR flux distribution of the signal under the assumption that the neutrino flux is proportional to the IR flux of the echo.

The TS for our full dataset of 36 neutrinos and 63 accretion flares is given by the sum of

TS_i. For spatial coincidence we require that the flare coordinates are within the 90% CL sky area of the neutrino. Our definition of temporal coincidence is that the neutrino arrived while the transient was still detected in ZTF and NEOWISE observations, with a maximum neutrino lag of 1 year with respect to the optical peak. We find TS$= 32.6$ for our sample, with contributions from three neutrino-flare pairs. By repeatedly redistributing accretion flares randomly over the ZTF sky and redoing the likelihood analysis, we find that about 1 in 5000 of such realizations yield a TS value that is at least as large: $p = 1.9 \times 10^{-4}$ corresponding to a significance of 3.7σ.

Similar to the approach used for the blazar TXS 0506+056 (*3*), our analysis is not blind because the likelihood function was defined after two neutrino associations were established (AT2019dsg and AT2019fdr). However, these associations were obtained using only ZTF optical observation. The relevant IR data were released in March 2021, and therefore the echo strength was not used to establish the neutrino coincidence. Yet both AT2019dsg and AT2019fdr have the strongest dust echoes of all ZTF flares (Fig. 2). Thanks to this obvious property, the choices of the likelihood method (Eq. 1) have only a limited effect on the final outcome, as evidenced by the similar probability for the background hypothesis obtained using solely a density-based expectation value (see Supplement). In this work we develop a new hypothesis, namely that accretion flares with dust echoes are sources of neutrino emission. We tested this hypothesis with a sample of 36 neutrinos (compared to 24 that were used to find AT2019dsg and AT2019fdr), uncovering a third flare (AT2019aalc) that has the highest dust echo flux of all ZTF transients. Additional, independent evidence for the associations follows from the multi-wavelength properties of the three neutrino sources.

The previously detected accretion flares coincident with high-energy neutrinos were accompanied by unusually soft X-ray emission (*10, 11*). Likewise, using SRG/eROSITA observations obtained after the optical peak of AT2019aalc, we measure a soft thermal spectrum with temperature of $kT = 172 \pm 10$ eV. Such soft thermal emission is rare: using SRG/eROSITA observa-

tions of 84 accretion flares with potential dust echoes, we find that $< 13\%$ of these are as soft as AT2019aalc ($kT < 172$ eV), and even fewer are as soft as AT2019dsg and AT2019fdr. These distinctive X-ray properties provide independent 3σ ($p = 0.13^3$) evidence for the hypothesis that accretion flares are correlated with high-energy neutrinos.

Another shared property of the three events is low-luminosity radio emission. Archival radio observations at the location of AT2019aalc (*15, 16*) show an unresolved source with a luminosity of $3 \times 10^{38}\,\mathrm{erg\,s^{-1}}$ at 1.4 GHz and an optically thin spectral index of -1. These pre-flare detections imply that, similar to AT2019fdr, the radio emission is not directly related to the optical flare. Nevertheless, these radio detections demonstrate that the black hole was able to produce a jet or outflow in its recent past. Jet production by black holes likely requires sufficient magnetic flux near the black hole horizon (*17*) and not all accreting black holes are able to reach this state. Less than 10% of the accretion flares with potential dust echoes in our sample of candidate dust echoes are detected in archival (*15, 16*) radio observations.

Taken together, the shared X-ray, radio, and optical properties of the three flares with neutrino coincidences (Fig. 3) point to a new population of cosmic particle accelerators. About half of the neutrinos in the IceCube alerts dataset are expected to be background (atmospheric) events. Based on the "signalness" probability (*8*) of the neutrinos in our sample, we expect about 16 astrophysical neutrinos in our sample. Hence three coincident events implies that at least $19^{+22}_{-12}\%$ (90%CL) of the IceCube astrophysical neutrino alerts are explained by accretion flares in our sample. This estimate will increase by a factor ~ 2 after applying a correction for the incompleteness of our sample (*10*) to obtain the fraction of astrophysical neutrino alerts produced by the entire accretion flare population.

A sizable contribution of accretion flares to the cosmic neutrino flux is remarkable because the volumetric energy injection of these flares is much lower than the energy output of regular AGN. For example, the sum of the IR echo flux of the accretion flares is 0.1 Jy, while the sum of

the baseline IR flux of the AGN detected by ZTF is 10 Jy. At radio wavelengths this difference in the received energy is even larger.

Given that steady AGN outshine accretion flares by at least two orders of magnitude we reach a clear conclusion: in order to explain the observed PeV-scale neutrino associations, the accretion flares must be vastly more efficient particle accelerators than the majority of AGN.

The fact that accretion flares are a cosmic minority presents a challenge for models of TDEs as neutrino sources that involve a relativistic jet (*18, 19*) or corona (*20*). Since AGN also have these features, equal efficiency of PeV-scale particle acceleration would imply that AGN produce a neutrino flux an order of magnitude larger than the total flux observed by IceCube. Different boundary conditions for efficient particle acceleration in TDE-induced jets could exist, but this appears unlikely given that two of the three accretion flares (AT2019fdr and AT2019aalc) occurred in AGN.

The low black hole mass of the accretion flares coincident with neutrinos points to a potential solution for the efficiency puzzle. Both TDEs and extreme AGN flares can reach the Eddington limit. Due to photon trapping, this high accretion rate makes the scale height of the accretion disk significantly larger compared to the common geometrically thin disk that is reached at Eddington ratios of $\approx 10\%$ (*21*). This state change is supported by observations: the X-ray spectra of typical AGN are hard and non-thermal, while TDE and extreme AGN flares have thermal and soft X-ray spectra (*22, 23*).

Because geometrically thin disks have a low temperature and are radiatively efficient, the gas particles in these disks have a Maxwellian distribution, which disables the second-order Fermi acceleration. However, a super-Eddington accretion flow with a strong magnetic field ($\gtrsim 10^5$ G, see Supplement) can make PeV-scale particle acceleration possible (*24*). Because the disk environment will absorb the gamma-ray emission produced in π^0 decay through the pair-creation process (*20, 24*), a disk-based particle accelerator is predicted to be dark above

GeV energies, consistent with the upper limits on gamma-ray emission for the three accretion flares with neutrino matches (Table 1).

The strong magnetic field required for accelerating protons up to PeV energies could be hosted in a relic disk that lingered after a prior episode of accretion onto the black hole. Alternatively, a high B-field could be provided by the tidal disruption of a red giant star with a strongly magnetized core (*25*) or of a strongly magnetized merger product of two high-mass stars (*26*). In the latter scenario, we may expect an increased amount of circumnuclear dust due to star formation, which provides a potential explanation for the ten times higher infrared luminosity of AT2019dsg compared to other TDEs without neutrino counterparts.

To conclude, the detection of three neutrinos from the rare population of accretion flares can be explained if the particle acceleration efficiency drastically increases towards the Eddington limit and a magnetic field with a strength of $\sim 10^5$ G is available near the black hole. In analogy with X-ray binaries that show radio flares as they change from low to high accretion rates (*27*), a different accretion state with a strong magnetic field can also explain why all three neutrino-emitting accretion flares in our sample are detected at radio wavelengths. In addition, this model provides an explanation for neutrino emission from NGC 1068, the most significant hotspot in the IceCube sky map at sub-PeV energies, detected at 2.9σ post-trial (*28*). NGC 1068 is exceptional because it is the nearest example of the rare subset of AGN accreting near the Eddington limit (*29, 30*), similar to the accretion flares presented in this work.

If we narrow the scope of our signal hypothesis to include only flares with evidence for super-Eddington accretion ($f_{\rm Edd} > 0.5$, based on their IR light curves), our likelihood method (Eq 1) yields a modestly higher significance for the neutrino correlation (3.8σ). Going forward, a study of the full IceCube neutrino archive together with an all-sky sample of super-Eddington flares or persistent super-Eddington AGN can further establish this new population of neutrino sources.

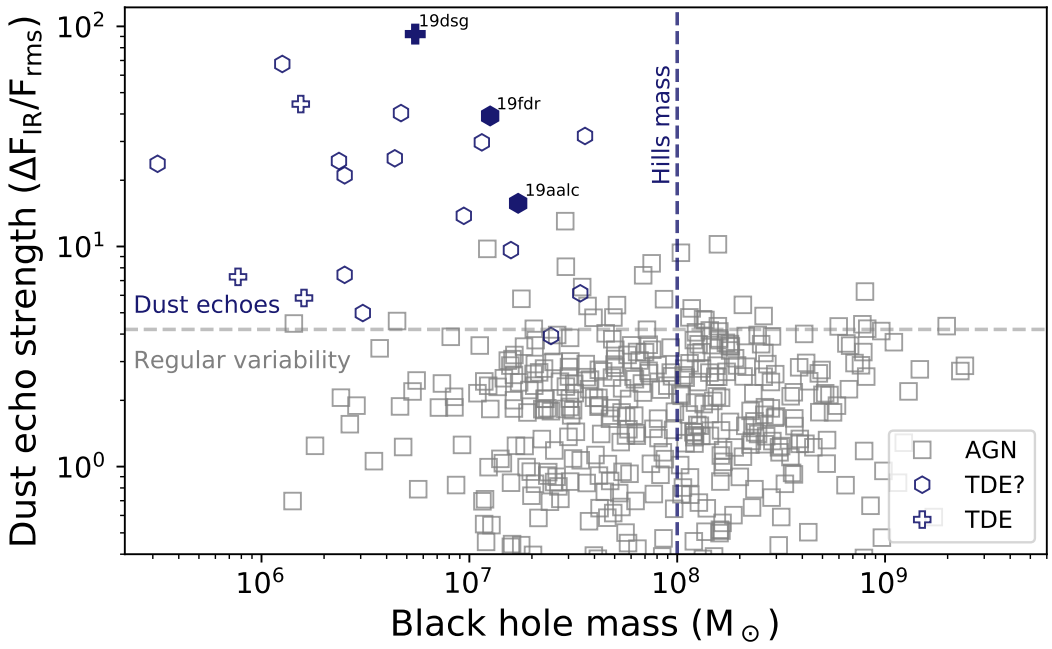

Figure 1: **Significant dust echoes occur almost exclusively in low-mass black holes**. The onset of strong echoes, measured using the infrared flux increase within one year of the optical peak of the flare, coincides with the Hills mass (*31*) for a solar-type star (defined by the requirement that the tidal radius is larger than the black hole horizon). For flares from active galaxies with broad emission lines in their optical spectra, the black hole mass is estimated from the width of the Hβ line and the luminosity (*32*), while for flares from inactive galaxies the velocity dispersion of the stars is used to estimate the black hole mass (*33*). The three accretion flares coincident with a high-energy neutrino are indicated with solid symbols.

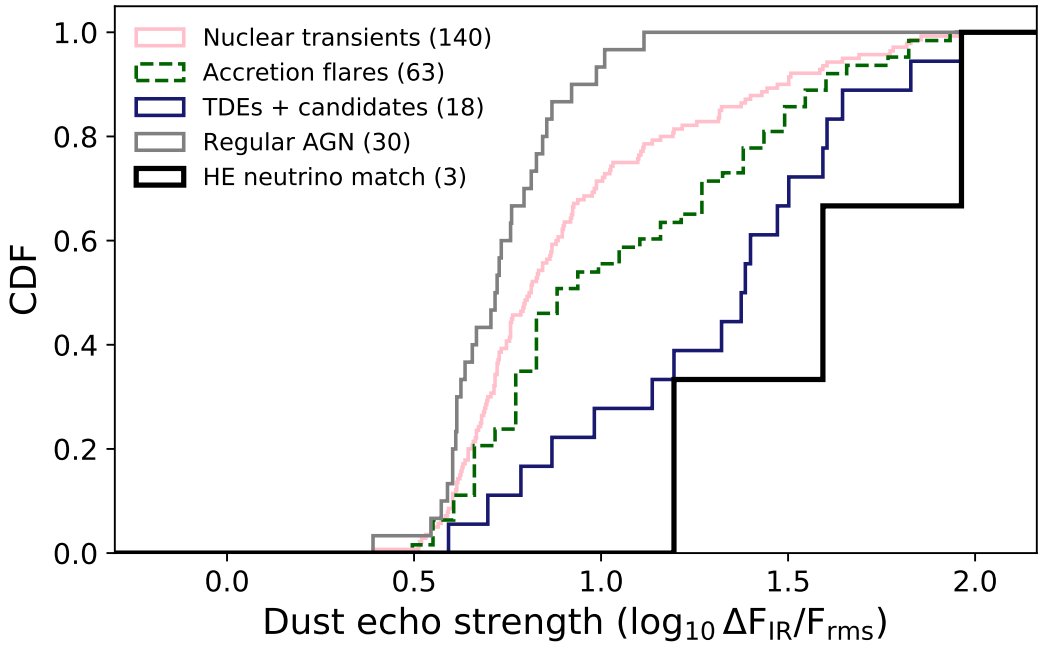

Figure 2: **Flares coincident with high-energy neutrinos have very strong dust echoes**. The TDE candidates (blue line) are defined as accretion flares with an estimated black hole mass (Fig. 1) below $10^8\ M_\odot$. This population shows much stronger dust echoes compared to regular variability from the AGN population (grey line). The echo strength distribution of the three neutrino-emitting events (black line) is inconsistent ($p = 0.007$ for an Anderson-Darling test) with originating from the population of all nuclear transients with detected dust echoes (pink line).

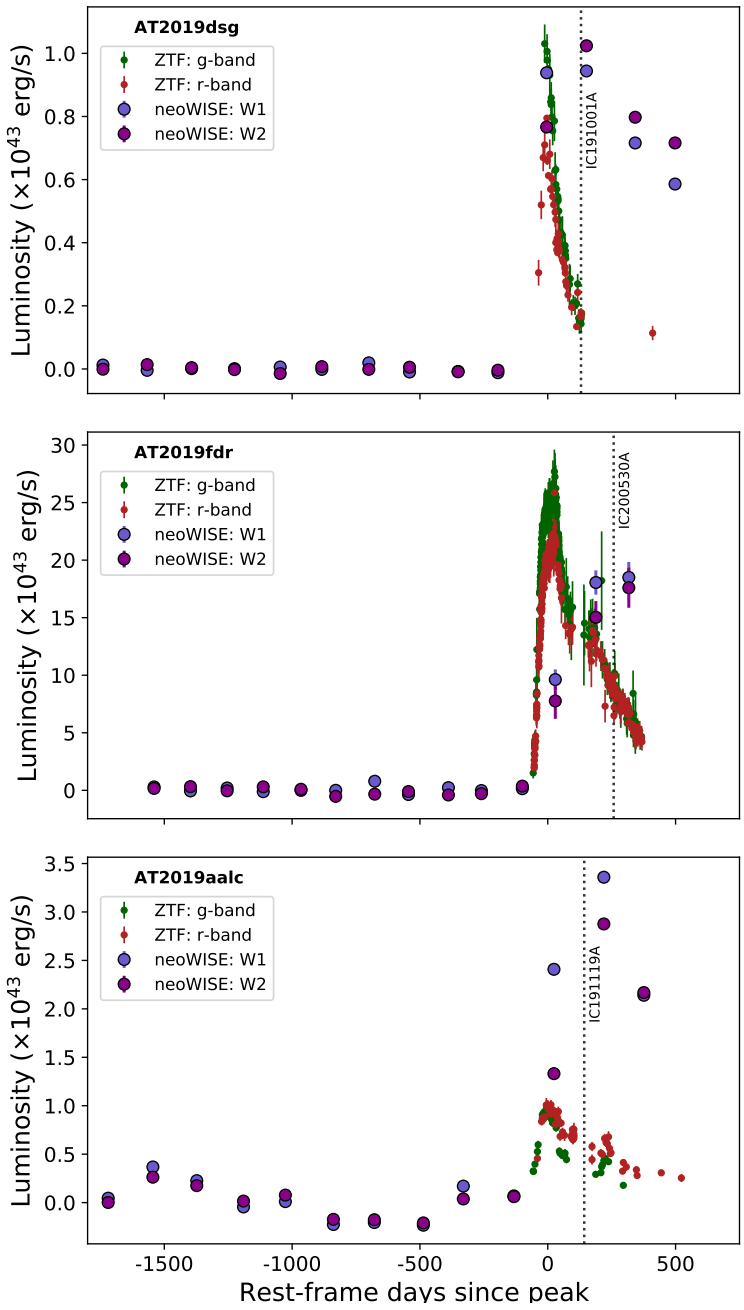

Figure 3: **Delayed neutrino detections for three accretion flares.** For each source, the neutrino arrived (dotted vertical lines) a few months after the peak of the optical light curve (red and green symbols). This delay can be explained by a constant particle acceleration efficiency during the first $\sim$ 1 year of the flare (*10*). The infrared light curve (blue and purple symbols) evolves on longer timescales due to the large distance of the dust sublimation radius (~ 0.1 pc). From the duration of the dust reverberation signal we infer a peak luminosity near the Eddington limit for all three flares (Table 1).

Flare name	Neutrino name	z	Δt days	Δd deg	X-ray temp. keV	*Fermi* limit $\mathrm{erg/s/cm^2}$	M_{BH} $M_\odot$	f_{Edd}
AT2019dsg	IC191001A	0.051	150	1.3	0.07 ± 0.01	$10^{-11.7}$	$10^{6.7}$	3.1
AT2019fdr	IC200530A	0.267	393	1.7	0.06 ± 0.03	$10^{-12.0}$	$10^{7.1}$	0.5
AT2019aalc	IC191119A	0.036	148	1.9	0.17 ± 0.01	$10^{-11.2}$	$10^{7.2}$	0.6

Table 1: **Multi-messenger inference.** The time difference of the neutrino arrival (Δt) is measured relative to the optical peak of the light curve. The angular offset (Δd) is measured relative to best-fit neutrino position (Table 3). The 95CL% upper limit on the flux measured by the *Fermi*-LAT telescope covers photons in the energy range 0.1–800 GeV (using an integration time relative to the neutrino arrival, see Supplement). The black hole mass (M_{BH}) is estimated from the optical spectrum of the host galaxy or the flare. The Eddington ratio (f_{Edd}) follows from the bolometric luminosity as obtained from the duration of the dust echo.

Acknowledgements – We acknowledge useful discussions and suggestions from J. Becerra González, M. Kerr, W. Lu, K. Murase, and W. Winter.

Based on observations obtained with the Samuel Oschin Telescope 48-inch and the 60-inch Telescope at the Palomar Observatory as part of the Zwicky Transient Facility project. ZTF is supported by the National Science Foundation under Grant No. AST-1440341 and Grant No. AST-2034437 and a collaboration including Caltech, IPAC, the Weizmann Institute for Science, the Oskar Klein Center at Stockholm University, the University of Maryland, the University of Washington, Deutsches Elektronen-Synchrotron and Humboldt University, Los Alamos National Laboratories, the TANGO Consortium of Taiwan, the University of Wisconsin at Milwaukee, Trinity College Dublin, Lawrence Livermore National Laboratories, and IN2P3, France. Operations are conducted by COO, IPAC, and UW. SED Machine is based upon work supported by the National Science Foundation under Grant No. 1106171.

This work is based on observations with the eROSITA telescope on board the SRG observatory. The SRG observatory was built by Roskosmos in the interests of the Russian Academy of Sciences represented by its Space Research Institute (IKI) in the framework of the Russian Federal Space Program, with the participation of the Deutsches Zentrum für Luft- und Raumfahrt (DLR). The SRG/eROSITA X-ray telescope was built by a consortium of German Institutes led by MPE, and supported by DLR. The SRG spacecraft was designed, built, launched, and is operated by the Lavochkin Association and its subcontractors. The science data are downlinked via the Deep Space Network Antennae in Bear Lakes, Ussurijsk, and Baykonur, funded by Roskosmos. The eROSITA data used in this work were processed using the eSASS software system developed by the German eROSITA consortium and proprietary data reduction and analysis software developed by the Russian eROSITA Consortium.

This work includes data products from the Near-Earth Object Wide-field Infrared Survey Explorer (NEOWISE), which is a project of the Jet Propulsion Laboratory/California Institute

of Technology. NEOWISE is funded by the National Aeronautics and Space Administration.

The *Fermi*-LAT Collaboration acknowledges support for LAT development, operation and data analysis from NASA and DOE (United States), CEA/Irfu and IN2P3/CNRS (France), ASI and INFN (Italy), MEXT, KEK, and JAXA (Japan), and the K.A. Wallenberg Foundation, the Swedish Research Council and the National Space Board (Sweden). Science analysis support in the operations phase from INAF (Italy) and CNES (France) is also gratefully acknowledged. This work performed in part under DOE Contract DE-AC02-76SF00515.

MG, PM and RS acknowledge the partial support of this research by grant 21-12-00343 from the Russian Science Foundation. KH has been supported by the Basic Science Research Program through the National Research Foundation of Korea (NRF) funded by the Ministry of Education (2016R1A5A1013277 and 2020R1A2C1007219), and also financially supported during the research year of Chungbuk National University in 2021. YY thanks the Heising–Simons Foundation for financial support. SR was supported by the Helmholtz Weizmann Research School on Multimessenger Astronomy, funded through the Initiative and Networking Fund of the Helmholtz Association, DESY, the Weizmann Institute, the Humboldt University of Berlin, and the University of Potsdam. ECK acknowledges support from the G.R.E.A.T research environment funded by *Vetenskapsrådet*, the Swedish Research Council, under project number 2016-06012, and support from The Wenner-Gren Foundations. MMK acknowledges generous support from the David and Lucille Packard Foundation. This work was supported by the GROWTH project funded by the National Science Foundation under Grant No 1545949.

References

1. K. Murase, *Active Galactic Nuclei as High-Energy Neutrino Sources* (2017), pp. 15–31.

2. G. R. Farrar, A. Gruzinov, *Astrophys. J.* **693**, 329 (2009).

3. IceCube Collaboration et al., *Science* **361**, eaat1378 (2018).

4. M. G. Aartsen, *et al.*, *Astrophys. J.* **835**, 45 (2017).

5. M. Aartsen, *et al.*, *Physical Review Letters* **124** (2020).

6. IceCube Collaboration, *Science* **342**, 1242856 (2013).

7. I. Bartos, D. Veske, M. Kowalski, Z. Marka, S. Marka, *arXiv e-prints* p. arXiv:2105.03792 (2021).

8. M. G. Aartsen, *et al.*, *Astroparticle Physics* **92**, 30 (2017).

9. E. C. Bellm, *et al.*, *Publ. Astron. Soc. Pac.* **131**, 018002 (2019).

10. R. Stein, *et al.*, *Nature Astronomy* **5**, 510 (2021).

11. S. Reusch, R. Stein, M. Kowalski, et al., *in prep* (2021).

12. S. van Velzen, *et al.*, *Astrophys. J.* **908**, 4 (2021).

13. A. Mainzer, *et al.*, *Astrophys. J.* **792**, 30 (2014).

14. S. van Velzen, D. R. Pasham, S. Komossa, L. Yan, E. A. Kara, *Space Sci. Rev.* **217**, 63 (2021).

15. R. H. Becker, R. L. White, D. J. Helfand, *Astrophys. J.* **450**, 559 (1995).

16. M. Lacy, *et al.*, *Publ. Astron. Soc. Pac.* **132**, 035001 (2020).

17. R. D. Blandford, R. L. Znajek, *Mon. Not. R. Astron. Soc.* **179**, 433 (1977).

18. G. R. Farrar, T. Piran, *arXiv e-prints* p. arXiv:1411.0704 (2014).

19. W. Winter, C. Lunardini, *Nature Astron.* **5**, 472 (2021).

20. K. Murase, S. S. Kimura, B. T. Zhang, F. Oikonomou, M. Petropoulou, *Astrophys. J.* **902**, 108 (2020).

21. M. A. Abramowicz, P. C. Fragile, *Living Reviews in Relativity* **16**, 1 (2013).

22. R. Saxton, S. Komossa, K. Auchettl, P. G. Jonker, *Space Sci. Rev.* **216**, 85 (2020).

23. S. Frederick, *et al.*, *arXiv e-prints* p. arXiv:2010.08554 (2020).

24. K. Hayasaki, R. Yamazaki, *Astrophys. J.* **886**, 114 (2019).

25. J. Fuller, M. Cantiello, D. Stello, R. A. Garcia, L. Bildsten, *Science* **350**, 423 (2015).

26. F. R. N. Schneider, *et al.*, *Nature* **574**, 211 (2019).

27. R. P. Fender, T. M. Belloni, E. Gallo, *Mon. Not. R. Astron. Soc.* **355**, 1105 (2004).

28. M. G. Aartsen, *et al.*, *Phys. Rev. Lett.* **124**, 051103 (2020).

29. T. Kawaguchi, *Astrophys. J.* **593**, 69 (2003).

30. G. Lodato, G. Bertin, *Astron. Astrophys.* **398**, 517 (2003).

31. J. G. Hills, *Nature* **254**, 295 (1975).

32. H.-Y. Liu, *et al.*, *Astrophys. J. Suppl.* **243**, 21 (2019).

33. K. Gültekin, *et al.*, *Astrophys. J.* **698**, 198 (2009).

34. M. J. Graham, *et al.*, *Publ. Astron. Soc. Pac.* **131**, 078001 (2019).

35. R. Dekany, *et al.*, *Publ. Astron. Soc. Pac.* **132**, 038001 (2020).

36. A. Mainzer, *et al.*, *Astrophys. J.* **731**, 53 (2011).

37. E. L. Wright, *et al.*, *Astrophys. J.* **140**, 1868–1881 (2010).

38. S. van Velzen, *et al.*, *Astrophys. J.* **872**, 198 (2019).

39. F. J. Masci, *et al.*, *Publ. Astron. Soc. Pac.* **131**, 018003 (2019).

40. M. T. Patterson, *et al.*, *Publ. Astron. Soc. Pac.* **131**, 018001 (2019).

41. J. Nordin, *et al.*, *Astron. Astrophys.* **631**, A147 (2019).

42. E. Hammerstein, *et al.*, *Astrophys. J.* **908**, L20 (2021).

43. E. L. Wright, *et al.*, *Astron. J.* **140**, 1868 (2010).

44. W. Lu, P. Kumar, N. J. Evans, *Mon. Not. R. Astron. Soc.* **458**, 575 (2016).

45. S. van Velzen, A. J. Mendez, J. H. Krolik, V. Gorjian, *Astrophys. J.* **829**, 19 (2016).

46. R. D. Blandford, C. F. McKee, *Astrophys. J.* **255**, 419 (1982).

47. B. M. Peterson, *et al.*, *Astrophys. J.* **613**, 682 (2004).

48. J. Magorrian, *et al.*, *Astron. J.* **115**, 2285 (1998).

49. K. Gebhardt, *et al.*, *Astrophys. J.* **539**, L13 (2000).

50. L. C. Ho, M. Kim, *Astrophys. J.* **809**, 123 (2015).

51. D. G. York, *et al.*, *Astron. J.* **120**, 1579 (2000).

52. S. Frederick, *et al.*, *Astrophys. J.* **883**, 31 (2019).

53. J. B. Oke, *et al.*, *Publ. Astron. Soc. Pac.* **107**, 375 (1995).

54. J. B. Oke, J. E. Gunn, *Publ. Astron. Soc. Pac.* **94**, 586 (1982).

55. E. C. Bellm, B. Sesar, pyraf-dbsp: Reduction pipeline for the Palomar Double Beam Spectrograph (2016).

56. D. A. Perley, *Publ. Astron. Soc. Pac.* **131**, 084503 (2019).

57. M. Nicholl, *et al.*, *Mon. Not. R. Astron. Soc.* **499**, 482 (2020).

58. G. Cannizzaro, *et al.*, *Mon. Not. R. Astron. Soc.* **504**, 792 (2021).

59. M. M. Kasliwal, *et al.*, *Publ. Astron. Soc. Pac.* **131**, 038003 (2019).

60. N. Blagorodnova, *et al.*, *Publ. Astron. Soc. Pac.* **130**, 035003 (2018).

61. M. Rigault, *et al.*, *Astron. Astrophys.* **627**, A115 (2019).

62. C. Fremling, *et al.*, *Astrophys. J.* **895**, 32 (2020).

63. D. A. Perley, *et al.*, *Astrophys. J.* **904**, 35 (2020).

64. W. B. Atwood, *et al.*, *Astrophys. J.* **697**, 1071 (2009).

65. M. Wood, *et al.*, *35th International Cosmic Ray Conference (ICRC2017)* (2017), vol. 301 of *International Cosmic Ray Conference*, p. 824.

66. S. Abdollahi, *et al.*, *Astrophys. J. Suppl.* **247**, 33 (2020).

67. J. Ballet, T. H. Burnett, S. W. Digel, B. Lott, *arXiv e-prints* p. arXiv:2005.11208 (2020).

68. R. Sunyaev, *et al.*, *Astron. Astrophys in press,* p. arXiv:2104.13267 (2021).

69. P. Predehl, *et al.*, *Astron. Astrophys.* **647**, A1 (2021).

70. S. Sazonov, *et al.*, *Mon. Not. R. Astron. Soc.* (2021).

71. N. Gehrels, *et al.*, *Astrophys. J.* **611**, 1005 (2004).

72. C. Kopper, *GRB Coordinates Network* **24028**, 1 (2019).

73. R. Stein, *GCN Circular* **26655** (2020).

74. R. Stein, *GCN Circular* **27534** (2020).

75. K. D. Alexander, S. van Velzen, A. Horesh, B. A. Zauderer, *Space Sci. Rev.* **216**, 81 (2020).

76. C. D. Dermer, G. Menon, *High Energy Radiation from Black Holes: Gamma Rays, Cosmic Rays, and Neutrinos* (2009).

77. L. Stawarz, V. Petrosian, *Astrophys. J.* **681**, 1725 (2008).

78. C. D. Dermer, J. A. Miller, H. Li, *Astrophys. J.* **456**, 106 (1996).

79. S. S. Kimura, K. Murase, K. Toma, *Astrophys. J.* **806**, 159 (2015).

80. R. Narayan, I. V. Igumenshchev, M. A. Abramowicz, *Publ. of the Astron. Soc. of Jap.* **55**, L69 (2003).

81. M. J. Aschwanden, *Encyclopedia of the Solar System (Third Edition)*, T. Spohn, D. Breuer, T. V. Johnson, eds. (Elsevier, Boston, 2014), pp. 235–259, third edition edn.

82. J. F. Donati, J. D. Landstreet, *ARA&A* **47**, 333 (2009).

83. A. Tchekhovskoy, R. Narayan, J. C. McKinney, *Mon. Not. R. Astron. Soc.* **418**, L79 (2011).

84. J. C. McKinney, A. Tchekhovskoy, R. D. Blandford, *Mon. Not. R. Astron. Soc.* **423**, 3083 (2012).

85. A. Mummery, *arXiv e-prints* p. arXiv:2104.06212 (2021).

86. J. K. Cannizzo, W. Chen, M. Livio, *Astrophys. J.* **454**, 880 (1995).

87. M. J. Rees, *Nature* **333**, 523 (1988).

88. E. S. Phinney, *The Center of the Galaxy*, M. Morris, ed. (Dordrecht: Kluwer, 1989), vol. 136 of *IAU Symposium*, p. 543.

89. T. Piran, G. Svirski, J. Krolik, R. M. Cheng, H. Shiokawa, *Astrophys. J.* **806**, 164 (2015).

90. N. Roth, *et al.*, *Space Sci. Rev.* **216**, 114 (2020).

91. C. Bonnerot, N. Stone, *arXiv e-prints* p. arXiv:2008.11731 (2020).

92. K. Hayasaki, P. G. Jonker, *arXiv e-prints* p. arXiv:2107.03666 (2021).

93. C. Bonnerot, E. M. Rossi, G. Lodato, *Mon. Not. R. Astron. Soc.* **464**, 2816 (2017).

94. C.-H. Chan, T. Piran, J. H. Krolik, D. Saban, *Astrophys. J.* **881**, 113 (2019).

95. D. Thomas, *et al.*, *Mon. Not. R. Astron. Soc.* **431**, 1383 (2013).

96. E. Blaufuss, *GCN Circular* **23214** (2018).

97. E. Blaufuss, *GCN Circular* **23375** (2018).

98. E. Blaufuss, *GCN Circular* **24378** (2019).

99. E. Blaufuss, *GCN Circular* **24854** (2019).

100. M. Santander, *GCN Circular* **24981** (2019).

101. E. Blaufuss, *GCN Circular* **25057** (2019).

102. R. Stein, *GCN Circular* **25225** (2019).

103. M. Santander, *GCN Circular* **25402** (2019).

104. R. Stein, *GCN Circular* **25802** (2019).

105. E. Blaufuss, *GCN Circular* **25806** (2019).

106. R. Stein, *GCN Circular* **25913** (2019).

107. E. Blaufuss, *GCN Circular* **26258** (2019).

108. E. Blaufuss, *GCN Circular* **26276** (2019).

109. R. Stein, *GCN Circular* **26341** (2019).

110. R. Stein, *GCN Circular* **26435** (2019).

111. M. Santander, *GCN Circular* **26620** (2019).

112. R. Stein, *GCN Circular* **26696** (2020).

113. C. Lagunas Gualda, *GCN Circular* **26802** (2020).

114. E. Blaufuss, *GCN Circular* **27612** (2020).

115. M. Santander, *GCN Circular* **27651** (2020).

116. E. Blaufuss, *GCN Circular* **27787** (2020).

117. R. Stein, *GCN Circular* **27865** (2020).

118. E. Blaufuss, *GCN Circular* **27941** (2020).

119. C. Lagunas Gualda, *GCN Circular* **27950** (2020).

120. M. Santander, *GCN Circular* **27997** (2020).

121. R. Stein, *GRB Coordinates Network* **28210**, 1 (2020).

122. C. Lagunas Gualda, *GRB Coordinates Network* **28411**, 1 (2020).

123. E. Blaufuss, *GRB Coordinates Network* **28433**, 1 (2020).

124. C. Lagunas Gualda, *GRB Coordinates Network* **28468**, 1 (2020).

125. C. Lagunas Gualda, *GRB Coordinates Network* **28504**, 1 (2020).

126. E. Blaufuss, *GRB Coordinates Network* **28509**, 1 (2020).

127. C. Lagunas Gualda, *GRB Coordinates Network* **28532**, 1 (2020).

128. M. Santander, *GRB Coordinates Network* **28575**, 1 (2020).

129. E. Blaufuss, *GRB Coordinates Network* **28616**, 1 (2020).

130. C. Lagunas Gualda, *GRB Coordinates Network* **28715**, 1 (2020).

131. C. Lagunas Gualda, *GRB Coordinates Network* **28889**, 1 (2020).

A Flare selection and photometry

The parent sample for the 63 accretion flares with dust echoes used in the likelihood analysis is constructed from ZTF (*9, 34, 35*) and NEOWISE (*36, 37*) data.

As described in refs. (*12, 38*) processing of the ZTF alert stream (*39, 40*) to yield a sample of nuclear transients is done with AMPEL (*41*). The input streams include both public ZTF data (MSIP) and private partnership data. We remove events with a weighted host-flare offset (*38*) > 0.5". To be able to measure the properties of the light curve we require at least 10 ZTF detections. We also remove ZTF sources for which the majority of the light curve measurements have a negative flux relative to the reference image. These requirements leaves 3143 nuclear transients that occurred between 2018 and 2020.5, see Fig. 4.

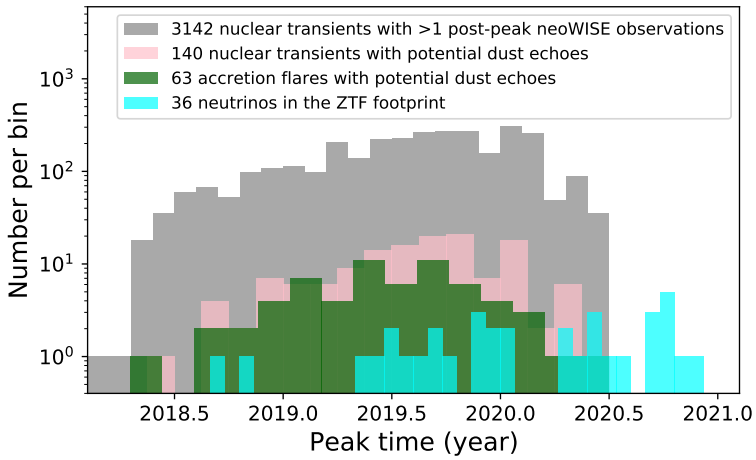

Figure 4: Distribution of the time of maximum light of the ZTF light curve and the neutrino arrival. The lack of ZTF events with a peak after mid-2020 happens because the NEOWISE data release includes observations up to the end of 2020 and to be able to measure the properties of the dust echo we require at least two post-peak detections in NEOWISE. Given the 6 month cadence of NEOWISE, the ZTF light curve has to peak prior to mid-2020 to meet this requirement. Because we allow the neutrino to arrive after the peak of the optical flare, all IceCube events up to the end of 2020 are included in the analysis.

To measure the peak flux of the ZTF light curve, we use the observation with the highest flux, after restricting to 90% of the data points with the highest signal-to-noise ratio (excluding 10% of lower quality data makes the peak estimate robust against outliers that occasionally occur in ZTF data).

To define our sample of accretion flares we use a requirement on the rise-timescale and fade-timescale of the ZTF light curve, see Fig. 6. These timescales are obtained from the measurements of van Velzen et al. (*12*) who applied a Gaussian-rise exponential-decay model to the ZTF alert photometry (both the g- and r-band are used in this fit). This model explicitly assumes that a single transient explains the entire ZTF light curve. When a light curve has multiple peaks of similar amplitude, the parameters of the fit reflect the (slower) timescale of the majority of the data points. We require a minimal amplitude of the flare of $\Delta m < -1$. In addition, we set an upper limit to the rise and fade timescale (e-folding time < 100 days and < 500 days, respectively). These cuts cast a wide net, and retrieve 1732 sources. About 15% of these are spectroscopically confirmed SN. The photometric selection recovers all ZTF TDEs and all large-amplitude flares from Seyfert galaxies that have been reported in earlier work (*12, 23, 42*).

The NEOWISE (*13*) light curves cover a period from 2016 to 2020. Most parts of the sky are visited every 6 months and receive about 10 observations within a 24 hour period of this visit (*43*). The inverse-variance weighted mean of the cataloged flux during these visits is used to construct the NEOWISE light curves. For each source, the baseline is defined using all NEOWISE observations obtained up to 6 months before the peak of the ZTF light curve. The 6 months padding is added to avoid including part of the dust echo signal into the baseline (e.g., when ZTF observations miss the onset of the flare).

To measure the echo strength we require two observations after the ZTF peak. We define the dust echo flux as $\Delta F_{\rm IR}$: the difference between the baseline flux and the mean NEOWISE

flux within one year after the ZTF peak. The echo strength is $\Delta F_{\rm IR}/F_{\rm rms}$, with $F_{\rm rms}$ the root-mean-square variability of the baseline observations. The significance of the rms variability is measured using the ratio $F_{\rm rms}/\sigma_F$, with σ_F the measurement uncertainty of the baseline observations. We selected candidate dust echoes by requiring that the echo strength is larger than the significance of the baseline rms variability: $\Delta F/F_{\rm rms} > F_{\rm rms}/\sigma_F$. We apply this criterion to both W1 and W2 light curves, which leaves 140 nuclear transients.

In Fig. 5 we show the echo flux and luminosity versus echo strength. We summarise their properties in Table 2.

In Fig. 3 of the main text we show the NEOWISE and ZTF light curves of the three flares coincident with a high-energy neutrino. For infrared emission due to reverberation, the energy emitted by the dust cannot exceed the integrated bolometric luminosity of the flare. For this reason, the lower optical-to-infrared ratio of the third source, AT2019aalc, likely implies a larger bolometric correction for its optical emission. This suggests ~ 1 mag of optical extinction in the host galaxy.

The time difference between the optical and IR light curve peaks yields an estimate of the inner radius of dust reprocessing region. At this dust sublimation radius, the bolometric flux absorbed by the dust is equal to the infrared luminosity emitted by the dust. We can therefore estimate the bolometric luminosity of the flare from the duration of the IR reverberation light curve (*14, 44, 45*). Using this geometric luminosity estimate (Eq. 12 in ref (*45*)), we find a bolometric luminosity $\sim 10^{45}\,{\rm erg}\,s^{-1}$ for all accretion flares coincident with high-energy neutrinos. All are consistent with reaching the Eddington limit (Table 1).

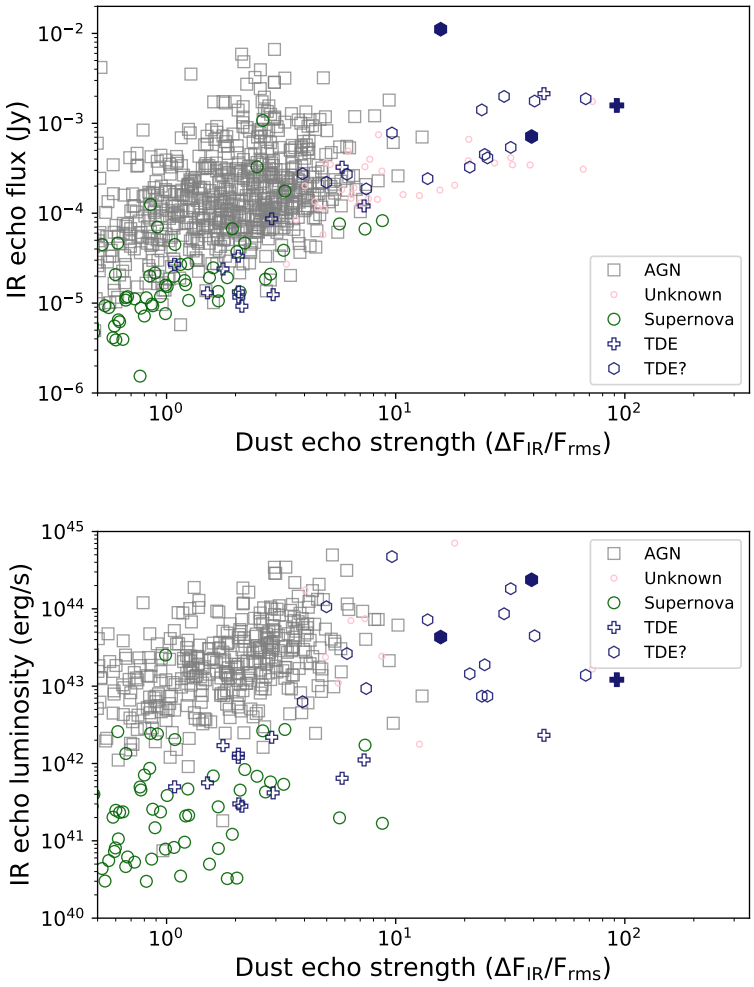

Figure 5: The dust echo luminosity and flux of nuclear transients in ZTF. We see that the three accretion flares coincident with a high-energy neutrino (filled symbols) are among the most powerful dust echoes in the sky.

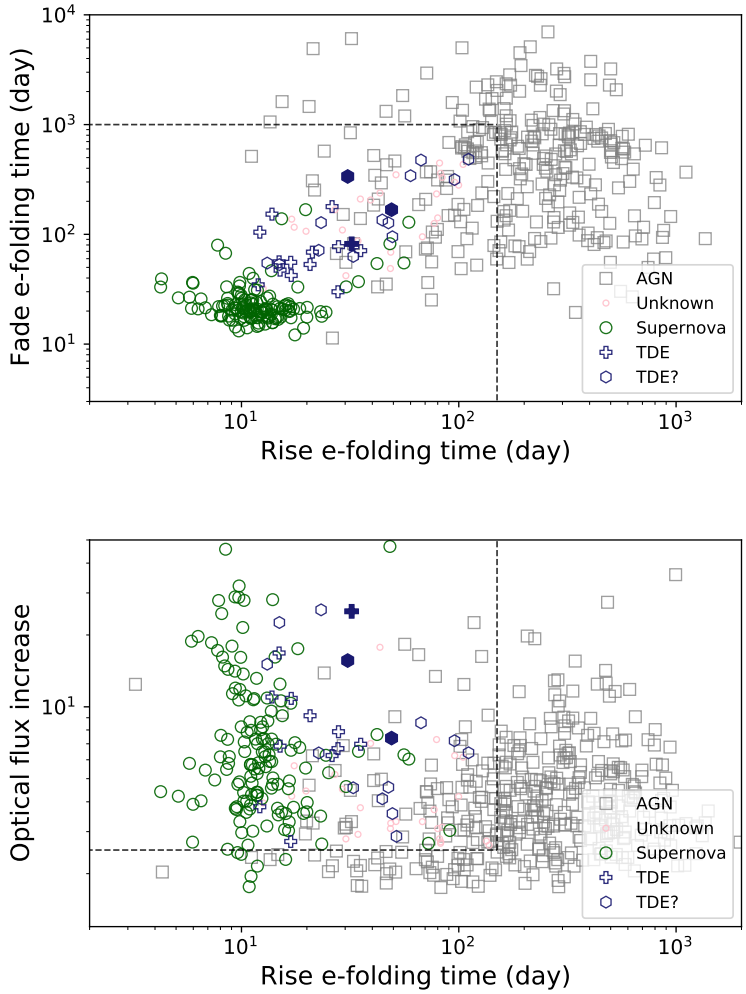

Figure 6: Parameters inferred from a Gaussian rise plus exponential decay model applied to the ZTF light curves. The flux increase is measured relative to the ZTF reference image. The dashed lines indicates the box that is used to separate accretion flares from regular AGN variability. This requirement selects nuclear supernovae, plus all known spectroscopically-confirmed ZTF TDEs. The three events coincident with a high-energy neutrino have solid plot symbols.

B Optical spectroscopy and black hole mass estimates

The black hole mass estimates shown in Fig. 1 are derived using two different methods: a relation based on reverberation mapping (*46, 47*) also known as "virial mass estimates", or the M–σ relation (*48, 49*). We use the former for spectra of type I AGN, i.e., sources that show broad Balmer emission lines in their optical spectrum. The M–σ relation is used for sources without broad emission lines that have a host galaxy spectrum with a measurement of the velocity dispersion of the stars.

For the reverberation method, a measurement of the size of the broad-line region in combination with the velocity of the emission lines yields an estimate of the black hole mass. This distance of the broad-line region to the black hole is not measured directly, but follows from the observed disk luminosity. We adopt the relation from (*50*):

$$\log M_{\rm BH} = \log \left[\left(\frac{\rm FWHM\ (H\beta)}{1000\ {\rm km\ s^{-1}}} \right)^2 \left(\frac{L_{5100}}{10^{44}\,{\rm erg\,s^{-1}}} \right)^{0.533} \right] + 6.91. \quad (2)$$

Here L_{5100} is the continuum luminosity at 5100 Å in the rest frame.

For active galaxies with spectra from the Sloan Digital Sky Survey (SDSS, (*51*)) we use the catalog of (*32*), who selected 14,584 type 1 AGN based on detection of a broad Hα line and applied Eq. 2 to measure the black hole mass. We find 580 nuclear transients with black hole mass estimates based on this catalog. Of these, eight are classified as accretion flares with potential dust echoes. In addition, spectroscopic follow-up observations of ZTF transients have yielded nine more type I AGN, six of these have been published (*23, 52*) and three are presented for the first time in this work: AT2019meh (ZTF19abclykm), AT2020afab (ZTF19abkdlkl), and AT2020iq (ZTF20aabcemq). We also obtained a new post-peak spectrum of AT2019aalc (Fig.7), which shows ongoing accretion two years after the peak of the optical flare.

The spectra of AT2020iq, AT2019meh, and AT2019aalc were obtained with the Low Resolution Imaging Spectrograph (LRIS; (*53*)) on the 10-m Keck-I telescope at 20, 660, and 714 days

post $t_{\rm peak}$ (Table 2), respectively. The new spectrum of AT2020afab was obtained with the Double Spectrograph (DBSP; (*54*)) on the 5-m Palomar telescope (P200) at 15 days post $t_{\rm peak}$. The DBSP spectrum was reduced with the `pyraf-dbsp` pipeline (*55*). The LRIS spectra were reduced using `Lpipe` (*56*).

For the remaining transients that have a velocity dispersion measurement based on a spectrum of the host galaxy, we apply the M–σ relation (*33*). This yields 219 additional $M_{\rm BH}$ measurements, of which five are classified as accretion flares with potential dust echoes. Of these five, three are based on archival SDSS spectra of the host galaxy and two are based on follow-up observations obtained after the flare has faded (*57, 58*). In Table 2, we list the reference for the black hole mass estimate for each accretion flare.

To keep track of the follow-up resources and spectroscopic classifications we used the GROWTH Marshal (*59*). Most of the supernova classifications (e.g. as shown in Fig. 6) are based on SEDM (*60, 61*) data and published in refs. (*62, 63*).

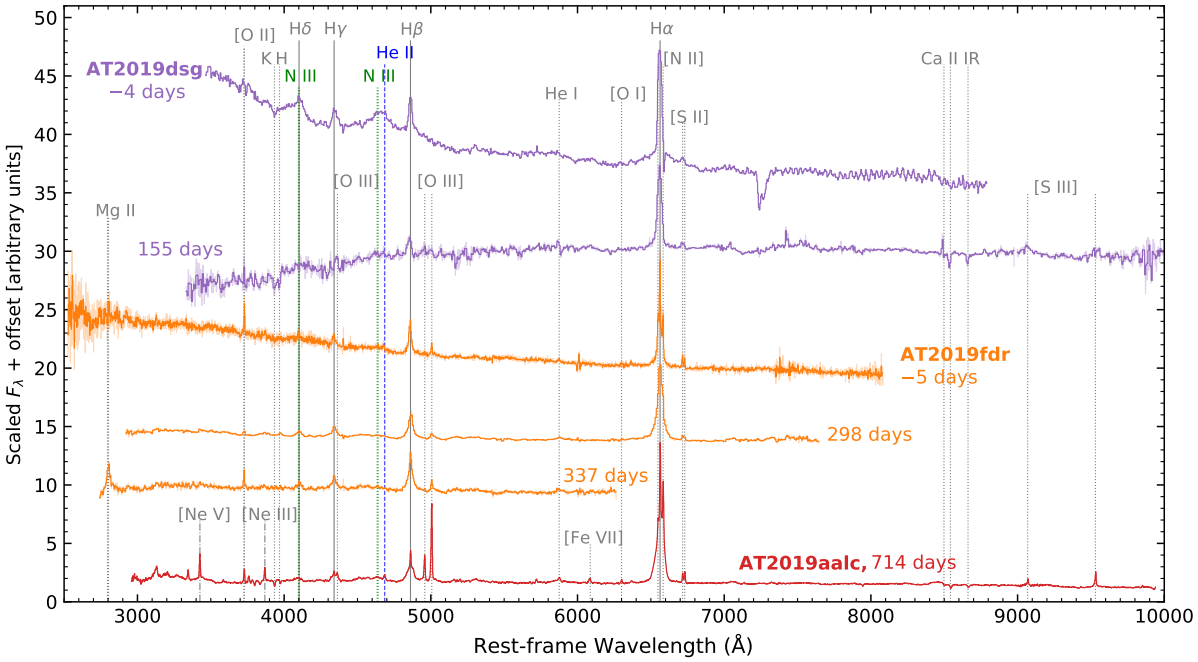

Figure 7: Optical spectra of the three accretion flares coincident with a high-energy neutrino. The observed time relative to the peak of the optical emission is indicated. Including data from (*10, 11, 23*).

C Gamma-ray analysis

We analysed data from the *Fermi* Large Area Telescope (*Fermi*-LAT) (*64*), a pair-conversion telescope sensitive to gamma rays with energies from 20 MeV to greater than 300 GeV. Following the approach outlined in (*10*), we use the photon event class from Pass 8 *Fermi*-LAT data (P8R3_SOURCE), and select a 15 $\times$ 15 deg region centered at the target of interest, with photon energies from 100 MeV to 800 GeV. We use the corresponding LAT instrument response functions P8R3_SOURCE_V2 with the recommended spectral models *gll_iem_v07.fits* and *iso_P8R3_SOURCE_V2_v1.txt* for the Galactic diffuse and isotropic component respectively, as hosted by the FSSC. We perform a likelihood analysis, binned spatially with 0.1 deg resolution and 10 logarithmically-spaced bins per energy decade, using the *Fermi*-LAT ScienceTools package (fermitools v1.2.23) along with the *fermipy* package v0.19.0 (*65*).

We studied the region of AT2019aalc in the time interval that includes 207 days of observations from the discovery of the optical emission on 2019 April 26 to the observation of the high-energy neutrino IC191119A on 2019 November 19). In this time interval, there is no significant ($\geq 5\sigma$) detection for any new gamma-ray source identified with a localization consistent with IC191119A. Two sources from the fourth *Fermi*-LAT point source catalog (4FGL-DR2 (*66, 67*)), consistent with the IC191119A localization, are detected in this interval. These are 4FGL J1512.2+0202 (4.1 deg from IC191119A), associated with the object PKS 1509+022, and 4FGL J1505.0+0326 (5.0 deg from IC191119A), associated with the object PKS 1502+036. The flux values measured for these two detections are consistent with the average values observed in 4FGL-DR2.

Likewise, we studied *Fermi*-LAT data of AT2019fdr using a time window from its discovery on 2019 May 3 to the arrival time of IC200530A on 2020 May 30. In this window, no gamma-ray sources were significantly ($\geq 5\sigma$) detected within the localization region of IC200530A,

neither previously known 4FGL-DR2 catalogued sources nor new gamma-ray excesses.

For both AT2019fdr and AT2019aalc, we test a point-source hypothesis at their position under the assumption of a power-law spectrum. The 95% CL upper limit for the energy flux (i.e., integrated over the whole analysis energy range) listed in Table 1 is derived for a power-law spectrum ($dN/dE \propto E^{-\Gamma}$) with photon power-law index $\Gamma = 2$. The *Fermi*-LAT upper limit for AT2019dsg listed in Table 1 is obtained using the same LAT data analysis strategy and covers a similar time window (150 days) relative to the optical discovery and the neutrino arrival time (*10*).

D SRG/eROSITA X-ray analysis

The SRG X-ray observatory (*68*) was launched to the halo orbit around Sun-Earth L2 point on July 13, 2019. On December 8, 2019 it started the all-sky survey, which will eventually comprise eight independent 6-month long scans of the entire sky. In the course of the sky survey, each point on the sky is being visited with the cadence of 6 months and the exposure and number of scans through the source depending on its ecliptic latitude. The eROSITA soft X-ray telescope (*69*) is operating in the 0.2-9 keV energy band with its effective area peaking at ≈ 1.5 keV.

As of October 2021, AT2019aalc (= SRGe J152416.7+045118) has been visited four times starting from February 2, 2020 with 6 month intervals and was detected in each scan. The X-ray light curve of the sources as seen by eROSITA, reached a plateau between August 2020 and January 2021 with the $0.3 - 2.0$ keV flux at $\approx 4.6 \times 10^{-13}$ erg s^{-1}cm^{-2}. The source had a soft thermal spectrum with the best fit blackbody temperature of $kT = 172 \pm 10$ eV.

The source AT2019fdr (= SRGe J170906.6+265124) has been visited four times starting from March 13, 2020. The sources was detected only once, on March 10–11, 2021, with the 0.3–2.0 keV flux of $\approx 6.0 \times 10^{-14}$ erg s^{-1}cm^{-2} and an extremely soft thermal spectrum with a

temperature of 56^{+32}_{-26} eV. This flare displayed the softest X-ray spectrum of all TDEs detected by eROSITA so far (*70*). In the three visits when the source remained undetected, the upper limit on its flux was in the range of $\sim (2-5)\times 10^{-14}$ erg s^{-1}cm^{-2}, assuming the same spectral shape as observed in the March 10–11, 2021 flare, see ref. (*11*) for details.

The source AT2019dsg has been visited by eROSITA three times starting from May 9, 2020 and so far remained undetected with the 3σ upper limit for the combined data of the three visits at a level of $\approx 1.9\times 10^{-14}$ erg/s/cm^2 (assuming a power law spectrum with the slope of $\Gamma = 1.8$). The X-ray spectral measurement of AT2019dsg listed in Table 1 are based on *Swift*/XRT (*71*) observations that were obtained closer to the optical peak of the flare (*10, 12*) than the eROSITA observations.

E IceCube alerts

The sample of 36 IceCube alerts used in this study is listed in Table 3. This list includes all published alerts (*8*) with a 90% confidence area that overlaps the ZTF footprint and a neutrino arrival date that allows a temporal match to our sample ZTF+NEOWISE accretion flares (see Fig. 4). We exclude the IceCube alerts that were subsequently retracted after the automated alert was issued. We also remove two events without a reported signalness (IC190331A (*72*) and IC200107A (*73*)) and one event with a 90%CL area larger than 300 deg^2 (IC200410A (*74*)).

F Likelihood analysis

We repeat here Eq. 1 of the main text for the test statistic (TS) of the ith neutrino:

$$\mathrm{TS}_i = 2\log\left[\left(\hat{S}/B\right)_{\mathrm{IC}}\left(\hat{S}/B\right)_{\mathrm{area}}\left(\hat{S}/B\right)_{\mathrm{echo}}\left(\hat{S}/B\right)_{\mathrm{flux}}\right] \tag{3}$$

This statistic is designed to test the hypothesis that accretion flares with dust echoes are a source of high-energy neutrinos. The signal associations can only occur if the neutrino is astrophysical, but background associations can occur regardless of the neutrino origin. When multiple flares matches to a single neutrino, the match with the highest signal ($\hat{S}$) is selected. When no matches are found, or the best-fit TS < 0, the background hypothesis ($S/B = 1$) is the best-fit. Below we discuss each term of Eq. 3 in more detail.

The first term is equal to the signalness of the IceCube alert $(S/B)_{\mathrm{IC}} = p_{\mathrm{signalness}}$. The signalness parameter is defined as $p_{\mathrm{signalness}} \equiv P_{\mathrm{signal}}/(P_{\mathrm{signal}} + P_{\mathrm{background}})$, with P_{signal} the probability that the observed track is explained by a muon produced by a cosmic neutrino and $P_{\mathrm{background}}$ the probability that the event has an atmospheric origin. For our signal hypothesis (that a given neutrino is correlated to an accretion flare) the neutrino must first be astrophysical. The null hypothesis is that the neutrino is not correlated to a flare. That could be because the neutrino arises from atmospheric background, or because the event is an astrophysical neutrino that does not originate from our source catalogue. Therefore, $(S/B)_{\mathrm{IC}} = p_{\mathrm{signalness}}$.

The second term of Eq. 3, $(S/B)_{\mathrm{area}}$, is the ratio of the signal to background expectation value based solely on the reconstructed position of the neutrino. A Monte Carlo approach is used to estimate the density of background sources. The first step is to obtain a probability distribution of the celestial coordinates of the ZTF extra-galactic transients. We use kernel density estimation to obtain a continuous probability distribution of the observed RA and Dec. from the positions of all ZTF transients from galaxies. We enforce a probability of zero for Galactic coordinates with $|b| < 8$ deg.

The sample of accretion flares used in our neutrino coincidence study contains 63 events (Table 2). Using the empirical probability distribution of the celestial coordinates, we redistributed these sources within the ZTF sky, creating one million pseudo sky-maps samples of 63 events. We then applied the same requirements for a spatial and temporal neutrino coincidence to each of these random samples. The mean areal density of background matches is given by the fraction of coincident events in the random samples over the total 90 %CL reconstruction area of the neutrinos. We find $n_{\rm ran} = 0.00073$ deg^{-2} (513,103 unique matches for 10^6 randomly distributed samples and a total neutrino area of 707 deg^2). For a given neutrino, the expected number of background coincidences is given by the product of $n_{\rm ran}$ and the 90 %CL area of the neutrino. Hence $(S/B)_{\rm area} = 0.9/n_{\rm ran}\Omega_{\rm IC}$.

Since our selection criteria for the accretion flares are inclusive rather than restrictive (Fig. 6), some regular AGN will also be included. In general, stronger echoes are less likely to be explained by normal AGN variability (Fig. 1), but rather by a single outburst or transient. The third term of Eq. 3, $(S/B)_{\rm echo}$ quantifies our belief that a given IR light curve is explained by a dust echo following a large amplitude accretion flare, rather than normal AGN variability. For the signal probability density function (PDF) we use the observed distribution of dust echo strength of TDE candidates (i.e., accretion flares from black holes with $M_{\rm BH} < 10^8\,M_\odot$). Comparing this to the dust echo strength distribution of the remaining accretion flares, we obtain an empirical estimate of $(S/B)_{\rm echo}$, see Fig. 8.

The final term in Eq. 3, $(S/B)_{\rm flux}$, depends only on the IR flux of the echo. If a neutrino-flare pair is due to a chance coincidence, this flux should follow the observed probability density function of echo flux of all 63 accretion flares. However, for real neutrino-flare coincidences we should expect more events from echoes with a larger flux; we expect the brightest sources to yield the first IceCube detections. In our sample of accretion flares, the top 5 represent 90% of the total echo flux of the population.

We can predict the signal term of $(S/B)_{\rm flux}$ using the assumption that the expectation value for the number of neutrino detections (i.e., the neutrino flux times the effective area of the telescope) is proportional to the IR flux of the echo. The echo flux is a reasonable proxy for the bolometric energy flux because dust efficiently absorbs the optical to soft X-ray emission of the flare and the re-emitted infrared emission is not affected by dust extinction in the host galaxy. However, the echo flux is also linearly proportional to the dust covering factor, which is not expected to be the same for each source. We compute the neutrino expectation value using $n_\nu \propto \Delta F_{\rm IR}$, with $\Delta F_{\rm IR}$ the dust echo flux. Applying this linear coupling to the observed echo flux distribution of the TDE candidates and drawing neutrino detections from a Poisson distribution with n_ν, we obtain a PDF for the IR flux distribution of accretion flares that can be expected to yield a neutrino alert. The result is shown in Fig. 9.

By redistributing the 63 accretion flares in the ZTF sky, we can measure the TS for the hypothesis that the neutrinos and accretion flares are not related. The fraction of the random samples that have a greater or equal TS compared to the observations yields the p-value of this null hypothesis. Using one million Monte Carlo samples we find $p = 1.9 \times 10^{-4}$. In Fig. 10 we show the distribution of the TS.

Each of the three events provides a roughly equal contribution to the TS. Repeating the calculation for the probability of the null hypothesis using each flare separately yields 0.03, 0.08, and 0.05 for AT2019dsg, AT2019fdr, and AT2019aalc, respectively.

The selection of accretion flares based on the ZTF properties of the light curve (rise time, fade time, amplitude; see Section A has a limited impact on the significance. If we select all nuclear transients with potential dust echoes (i.e., $\Delta F/F_{\rm rms} > F_{\rm rms}/\sigma_F$, yielding 140 sources), we still have the same three matches to IceCube alerts and our likelihood method gives $p = 3.3 \times 10^{-4}$.

As a cross-check on the robustness of our likelihood approach (Eq. 1), a simple yet in-

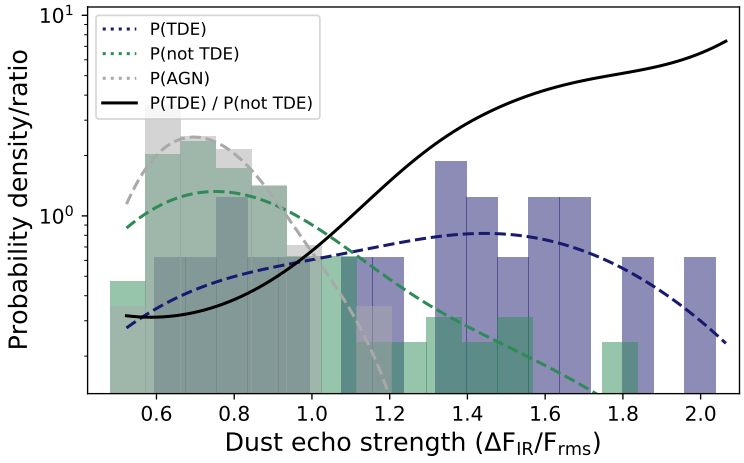

Figure 8: The observed distribution of dust echo strength for accretion flares with potential dust echoes. The *'TDE'* sample in this figures includes all accretion flares with $M_{\rm BH} < 10^8\,M_\odot$ and the *'not TDE'* population contains the remaining events. The observed distributions are approximated using using kernel density estimation with a bandwidth of 1 (dashed lines). The ratio of the resulting probability density functions (solid black line) is used in the likelihood analysis, namely $(S/B)_{\rm echo}$ in Eq. 1.

structive estimate of the significance can be obtained solely based on the low areal density of accretion flares with large dust echoes. We first note that for $\Delta F/F_{\rm rms} > 10$, the sample is dominated by TDE-like echoes (Fig. 1). Applying this cut on echo strength leaves 29 flares. From their duration we measure the probability for a temporal neutrino coincidence of 22%, thus finding an effective source density of $6.4/\Omega_{\rm ZTF}$, with $\Omega_{\rm ZTF} = 28 \times 10^3$ deg^2 the extragalactic sky seen by ZTF (*10*). Multiplying this source density with the total area covered by the IceCube neutrinos used in our analysis ($\sum \Omega_{\rm IC} = 706$ deg^2), we find that the expected number of chance associations is 0.16. The Poisson probability to see at least three events is 6×10^{-4}.

Using archival VLASS and FIRST radio data plus observations catalogued in (*75*), we measured that only 10-20% of the accretion flares in our sample are detected at radio wavelengths, compared to 100% of the three accretion flares with neutrino counterparts. If we decrease our

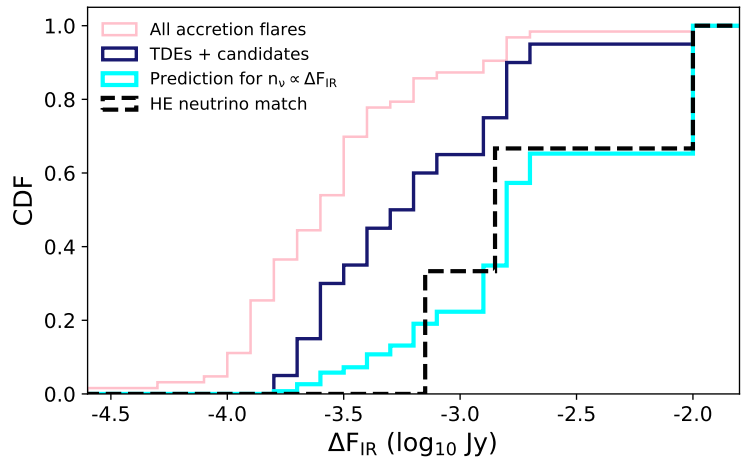

Figure 9: Cumulative distribution of the dust echo flux. To make a prediction for the flux distribution of accretion flares that are detected in a search for high-energy neutrinos, we assume that the expectation value for the number of neutrino detections from a given source is proportional to the echo flux. Applying this model to the observed echo flux distribution of accretion flares with $M_{\rm BH} < 10^8\,M_\odot$ yields the cyan curve. The ratio of the cyan and the pink PDFs is used for $(S/B)_{\rm flux}$ of Eq. 3. We see that the three flares coincident with a high-energy neutrino have a relatively high dust echo flux (in the top 80%), as expected for a real signal.

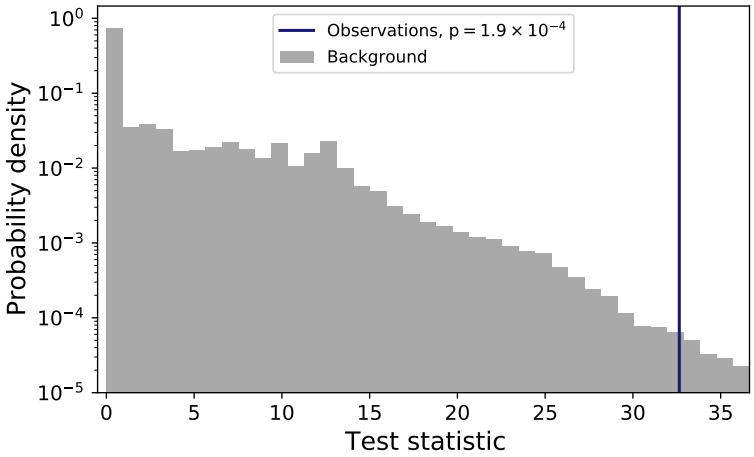

Figure 10: The distribution of the test statistics after redistributing the accretion flares in the ZTF sky. From this Monte Carlo simulation we find a probability $p = 1.9 \times 10^{-4}$ that the three accretion flares we associate with a high-energy neutrino are explained by a chance coincidence. The peak at zero is due to Monte Carlo realizations that yield zero coincident events.

estimate of the effective source density by 20% to include only radio-emitting sources, the Poisson probability to see at least three events becomes 5×10^{-6} corresponding to a significance of 4.4σ. Likewise, the effective source density can be decreased by a factor of 10 to account for the fact that all three sources with neutrino counterparts have a thermal X-ray spectrum (Table 1), yielding a significance of 4.8σ.

G Neutrinos from an Eddington-limited accretion disk

There are two main processes to produce high energy neutrinos ($E \gtrsim \mathrm{GeV}$): the photopion process and inelastic proton-proton collisions (*76*). The protons of the disk are scattered by turbulent magnetic fields and can accelerate stochastically to relativistic energies. The accelerated proton interacts with a thermal proton, producing a neutrino through pion decay. The resultant neutrino energy is given by $E_\nu = 0.05\, E_p$, where E_p is the accelerated proton's energy. Because, in a super-Eddington accretion flow, the photopion process works less efficiently than the inelastic proton-proton collisions, we consider here high-energy neutrino emission due to the inelastic interaction between thermal protons and relativistic protons energized through Fermi second-order stochastic acceleration.

The Fokker-Planck equation of the distribution function of non-thermal, relativistic protons yields the stochastic acceleration time, which is defined by p^2/D_p, where p and D_p are the proton momentum and diffusion coefficient (*77*). The acceleration time is obtained using the approximate diffusion coefficient (*78*):

$$t_{\mathrm{accl}} = \frac{1}{\zeta}\left(\frac{v_{\mathrm{A}}}{c}\right)^{-2}\left(\frac{r_{\mathrm{L}}}{R}\right)^{2-q}\frac{R}{c}\left(\frac{E_p}{m_p c^2}\right)^{2-q} \tag{4}$$

where $\zeta = 0.1$ is the ratio of the turbulent and non-turbulent magnetic fields, $v_{\mathrm{A}} = B/\sqrt{4\pi m_p n_p}$ is the Alfvén speed with a proton mass m_p and proton number density n_p, $q = 5/3$ is an index of the power spectrum of the magnetic turbulence, $r_{\mathrm{L}} = m_e c^2/(eB)$ is the Larmor radius with

an elementary charge e and an electron mass m_e, and R is the disk size (*79*).

The second-order Fermi acceleration is suppressed by various processes (e.g. mass accretion, proton-proton relaxation, Coulomb loss, photo-pion cooling, diffusion, proton-proton cooling, synchrotron cooling, Compton drag). For each process, the protons are accelerated to a maximum energy, which can be estimated by equating the acceleration timescale to the cooling timescale. However, if the magnetic field is large enough, the protons can reach PeV scales. For the very high B-field environment, three relevant cooling mechanisms for the Fermi acceleration remain: proton-proton cooling, synchrotron cooling, and Compton drag (*24*). The timescales are given by:

$$t_{\rm Sync} = 6\pi \left(\frac{m_p}{m_e}\right)^3 \left(\frac{E_p}{m_p c^2}\right)^{-1} \frac{m_e c^2}{c\sigma_{\rm T} B^2}, \tag{5}$$

for synchrotron cooling,

$$t_{pp} = \frac{1}{K_{pp}} \frac{1}{c\sigma_{pp} n_p}, \tag{6}$$

for proton-proton cooling, and

$$t_{\rm Cd} = \frac{3}{4} \frac{B^2}{U_\gamma} \frac{1}{c\sigma_T n_p} \quad , \tag{7}$$

for energy loss via Compton drag. In these equations, $\sigma_{\rm T}$ is the Thomson scattering cross section, $K_{pp} \sim 0.5$ is the proton inelasticity, $\sigma_{pp} \sim 4.2 \times 10^{-26}\,{\rm cm}^2$ for $E_p \sim 1\,{\rm PeV}$ is the total cross section of the proton-proton collision, and $U_\gamma \sim L_{\rm Edd} t_{\rm acc}/(4\pi R^3/3)$ is the radiation energy density of the Eddington limited disk.

Equating acceleration time Eq. (4) with Eqs. (5) to (7) and setting $E_p = 2\,(E_{\nu,{\rm obs}}/0.1\,{\rm PeV}){\rm PeV}$, we can estimate the required magnetic field strength as a function of proton number density, independently of the theoretical disk model. Fig. 11 shows the $B - n_p$ relation for given black hole mass and stellar mass, where the stellar radius is given through the mass-radius relation for a main-sequence star. The magnetic field strength of each process is indicated by $B_{\rm Sync}$, $B_{\rm pp}$,

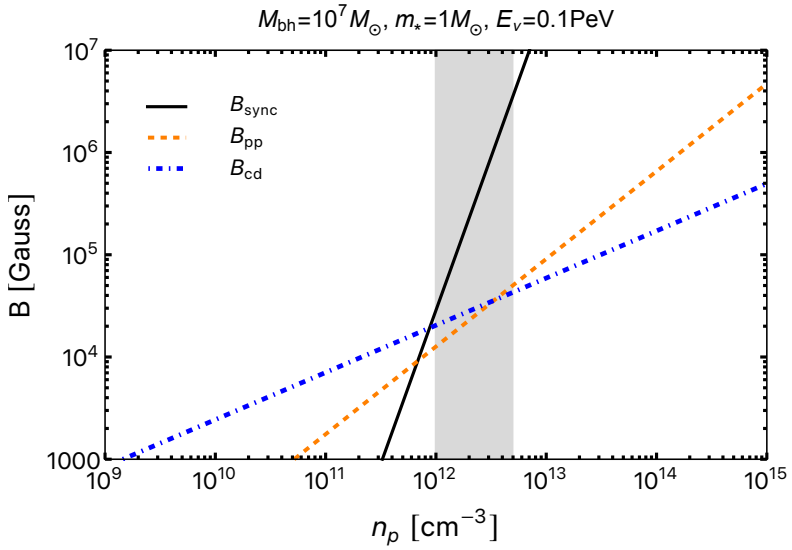

Figure 11: Magnetic field strength required to produce PeV neutrinos as a function of proton number density for a fixed black hole mass, stellar mass, and observed neutrino energy. For an Eddington-limited accretion flow, the three relevant mechanisms are: Synchrotron cooling (Eq. 5; black line), proton-proton cooling (Eq. 6; orange line), and Compton drag (Eq. 7; blue line). The gray shaded region represents the case for a super-Eddington MAD model (*24*).

and $B_{\rm Cd}$, respectively. Following the approach of Hayasaki et al. (*24*), the gray shaded region represents the case for a super-Eddington magnetically arrested disk (MAD) model. In a MAD flow, first proposed by (*80*), the magnetic field is strong enough to support the gas against the gravitational force acting on the disk. We adopt $0.01 \leq \epsilon \leq 0.05$ where ϵ is the ratio of radial diffusion to free-fall velocities; the width of the shaded area along the number density n_p of Fig. 11 is determined by this range of ϵ.

As shown in Fig. 11, the required B-field strength to reach sub-PeV neutrinos is $\sim 10^5$ G, which is several orders of magnitude larger than the background minimum B-field strength (~ 0.1 G) of a solar-type star (*81*). Young and massive stars are observed to host field strengths up to $\sim 10^4$ G on their surface (*82*). Based on stellar seismology, the core of a red giant star can reach a strong magnetic field of 10^{5-7} G (*25*). A merger of two massive main sequence

stars could result in fields of $\sim 10^7$ G in the core of the merger product (*26*). Hence the tidal disruption of a red giant or of a merger product can satisfy the required magnetic field for PeV proton acceleration. In the context of MADs, the origin of the B-field is thought to be a large-scale, poloidal magnetic field, which penetrates the whole disk vertically (*80*). Whether the magneto-rotational instability that locally works in the disk can produce this large scale magnetic field is an open challenge of numerical simulations (*83, 84*).

H Neutrino arrival delay

As shown in Fig. 3, a few months delay between the peak of the optical emission and the neutrino arrival is observed. For each of the three events, the delay is similar to the e-folding time of the optical light curve (Table 2). As such, a large part of the optical emission has been emitted by the time the neutrino arrives. It appears that the optical emission is not directly tracing the energy that is available for proton acceleration. Two explanations are possible.

If the mass accretion rate is constant over the first year, the neutrino flux is also expected to be constant. This constant neutrino flux means the probability to detect a single neutrino is constant over this period; a delayed detection is equally likely as a detection close to the optical peak. This explanation was used to explain the delayed neutrino detection of AT2019dsg, and is supported by the radio (*10*) and X-ray observations of this event (*85*).

Alternatively, the mass accretion rate may not be constant but decays with time following a power-law, t^{-n}. We have $1 \lesssim n \leq 5/3$; the low end of n is applicable for the disk-dominated phase (*85, 86*), whereas the high end is for the standard TDE case (*87, 88*). The optical/UV emission might not trace the accretion rate (*89*) and instead is emitted at the first shock of the stellar debris streams (*90*), which marks the onset of the debris circularization (*91*). The

circularization timescale of the most tightly bound debris can be estimated as (*92*)

$$t_{\rm circ} \approx 0.57\,\beta^{-3}\left(\frac{\eta}{0.1}\right)^{-1}\left(\frac{M_{\rm bh}}{10^7\,M_\odot}\right)^{-7/6}\left(\frac{m_*}{1\,M_\odot}\right)^{8/25}\ {\rm yr} \tag{8}$$

where $\eta\,(\leq 1)$ is the circularization efficiency which represents how efficiently the kinetic energy at the stream-stream collision is dissipated and the most efficient ($\eta = 1$) case corresponds to the result of ref. (*93*). Because the inner accretion disk is formed after the circularization of the debris, it could take of order $t_{\rm circ}$ for the first neutrinos to be produced, which match the observed time delay (Fig. 3). A caveat to Eq. 8 is a potential interaction of stellar debris stream with a pre-exisiting accretion disk, which can shorten the circularization timescale (*94*).

ZTF name	$t^a_{\rm peak}$ (MJD)	rise[b] (days)	fade[b] (days)	$\Delta F_{\rm IR}/F_{\rm rms}$	$\Delta F_{\rm IR}$ (mJy)	z	$M_{\rm BH}$ ($\log_{10} M_\odot$)	$\frac{P({\rm AGN})}{P({\rm TDE})}$[c]	spectro. class
AT2019dsg	58620.2	32.1	81.9	92.2	1.58 ± 0.02	0.0512	6.74 (C21)	0.000	TDE
AT2019fdr	58672.5	30.8	336.6	39.2	0.71 ± 0.07	0.2666	7.10 (F20)	0.000	TDE?
AT2019aalc	58658.2	49.0	167.7	15.7	11.13 ± 0.10	0.0356	7.23 (L19)	0.184	TDE?
AT2018dyk	58261.4	60.0	342.0	23.8	1.41 ± 0.03	0.0367	5.50 (F19)	0.005	TDE?
AT2019aame	58363.2	–	138.0	12.3	0.18 ± 0.01	–	–	0.557	–
AT2018lzs	58378.2	134.0	15.5	3.3	0.03 ± 0.01	–	–	4.144	–
AT2021aetz	58390.3	8.6	–	47.5	0.81 ± 0.01	0.0879	6.21 (T13)	0.000	TDE?
AT2018ige	58432.5	–	67.9	65.8	0.31 ± 0.01	–	–	0.000	–
AT2021aeud	58448.3	137.6	282.7	6.2	0.15 ± 0.01	–	–	4.288	–
AT2018iql	58449.4	17.9	41.0	30.1	0.48 ± 0.01	–	–	0.000	–
AT2018jut	58449.6	–	–	5.0	0.12 ± 0.01	–	–	5.782	–
AT2021aeue	58475.1	48.5	48.8	4.9	0.11 ± 0.01	–	–	5.881	–
AT2019aamf	58506.4	80.0	141.2	6.6	0.19 ± 0.01	–	–	3.744	–
AT2018kox	58510.2	26.9	167.6	5.6	0.33 ± 0.01	0.096	–	5.046	–
AT2018lhv	58513.5	17.5	116.1	32.3	0.35 ± 0.01	–	–	0.000	–
AT2019avd	58534.3	14.9	52.9	67.5	1.87 ± 0.05	0.0296	6.10 (F20)	0.000	TDE?
AT2016eix	58539.4	104.2	43.1	6.9	0.16 ± 0.01	–	–	3.277	–
AT2019aamg	58540.5	–	93.7	8.3	0.14 ± 0.00	–	–	1.945	–
AT2018lcp	58547.2	95.7	297.4	12.7	0.16 ± 0.01	0.06	–	0.495	–
AT2021aeuf	58556.4	17.0	137.5	15.6	0.18 ± 0.01	–	–	0.192	–
AT2020aezy	58558.4	82.5	359.8	4.8	0.06 ± 0.01	–	–	5.929	–
AT2019cle	58568.4	9.2	54.8	19.4	0.25 ± 0.01	–	–	0.041	–
AT2019aamh	58582.5	–	154.5	7.7	0.40 ± 0.01	–	–	2.459	–
AT2019dll	58605.2	29.6	–	6.8	0.26 ± 0.01	0.101	7.48 (T13)	3.461	TDE?
AT2019gur	58607.5	–	234.5	38.6	0.34 ± 0.01	–	–	0.000	–
AT2018lof	58608.2	70.9	370.4	4.1	0.15 ± 0.01	0.302	8.98 (L19)	5.974	AGN
AT2019dqv	58628.2	67.0	475.0	40.4	1.77 ± 0.02	0.0816	6.67 (L19)	0.000	TDE?
AT2019cyq	58637.2	49.5	95.0	31.8	0.54 ± 0.01	0.262	7.56 (L19)	0.000	TDE?
AT2021aeug	58641.2	48.6	68.8	4.6	0.11 ± 0.01	–	–	6.070	–
AT2019ihv	58646.5	–	19.3	8.7	0.29 ± 0.01	0.1602	–	1.687	–
AT2019dzh	58651.2	51.4	348.9	6.4	0.15 ± 0.01	0.314	–	4.007	–
AT2019kqu	58652.2	95.6	315.6	6.1	0.27 ± 0.01	0.174	7.53 (L19)	4.348	TDE?
AT2019hbh	58652.3	19.8	106.7	8.4	0.75 ± 0.01	–	–	1.880	–
AT2020aezz	58677.3	99.8	280.6	5.8	0.18 ± 0.01	–	–	4.771	–
AT2020afaa	58678.2	83.8	330.3	7.0	0.13 ± 0.02	–	–	3.187	–
AT2019idm	58682.2	51.7	–	25.2	0.41 ± 0.02	0.0544	6.64 (T13)	0.002	TDE?
AT2019ihu	58709.5	79.7	110.9	6.2	0.25 ± 0.02	0.27	8.90 (L19)	4.192	AGN
AT2019meh	58713.1	23.2	127.9	29.7	1.99 ± 0.04	0.0935	7.06 (V21)	0.000	TDE?
AT2020afab	58717.2	47.5	127.2	5.0	0.22 ± 0.01	0.2875	6.49 (V21)	5.789	TDE?
AT2019aami	58717.4	–	152.0	31.8	0.41 ± 0.01	–	–	0.000	–
AT2019nna	58717.4	34.4	87.1	27.0	0.36 ± 0.01	–	–	0.001	–
AT2019nni	58732.2	29.1	109.5	4.9	0.36 ± 0.01	0.137	–	5.834	–
AT2021aeuk	58733.1	43.4	238.1	7.3	0.33 ± 0.01	0.235	–	2.827	–
AT2019hdy	58749.5	–	87.9	4.0	0.20 ± 0.01	0.442	–	5.863	–
AT2019pev	58750.1	13.1	54.7	7.4	0.19 ± 0.01	0.097	6.40 (F20)	2.729	TDE?
AT2013kp	58753.1	11.9	34.7	44.4	2.14 ± 0.04	0.01499	6.19 (N20)	0.000	TDE
AT2019brs	58758.1	110.9	483.2	9.6	0.78 ± 0.01	0.3736	7.20 (F20)	1.227	TDE?
AT2020afac	58758.3	68.0	95.0	10.8	0.16 ± 0.01	–	–	0.865	–
AT2019wrd	58764.3	82.6	–	7.6	0.15 ± 0.01	–	–	2.562	–
AT2021aeuh	58789.5	–	–	3.9	0.28 ± 0.01	0.0834	7.39 (L19)	5.726	TDE?
AT2019msq	58791.2	137.9	–	6.4	0.16 ± 0.01	–	–	3.933	–

AT2019qpt	58798.3	44.5	135.1	13.8	0.24 ± 0.01	0.242	6.97 (L19)	0.355	TDE?
AT2020afad	58802.2	77.1	125.5	3.7	0.08 ± 0.01	–	–	5.217	–
AT2019mss	58811.6	35.2	209.7	20.8	0.38 ± 0.01	–	–	0.021	–
AT2019thh	58851.1	104.7	433.8	72.2	1.75 ± 0.02	0.0506	–	0.000	–
AT2021aeui	58860.3	–	60.0	6.2	0.49 ± 0.02	–	–	4.250	–
AT2020afae	58867.2	30.2	42.0	5.2	0.35 ± 0.02	–	–	5.585	–
AT2020mw	58867.3	12.6	32.1	6.8	0.12 ± 0.01	–	–	3.414	–
AT2020iq	58878.1	22.7	71.5	24.5	0.45 ± 0.01	0.096	6.37 (V21)	0.003	TDE?
AT2019xgg	58891.2	81.6	446.2	4.4	0.13 ± 0.01	–	–	6.091	–
AT2020atq	58903.2	39.3	205.5	20.8	0.66 ± 0.01	–	–	0.020	–
AT2021aeuj	58974.2	79.0	233.5	18.1	0.20 ± 0.01	0.695	–	0.071	–
AT2020hle	58978.3	32.7	62.9	21.0	0.33 ± 0.01	0.103	6.40 (F20)	0.018	TDE?

Table 2: **Optical/IR properties of the accretion flares.**
Notes – the first three entries of this table list the events coincident with an IceCube neutrino alert. [a]The column $t_{\rm peak}$ lists the time of maximum light of the ZTF light curve. [b]The rise and fade columns list the e-folding time. [c]The ratio of the AGN and TDE probability is based on the strength of the dust echo ($\Delta F_{\rm IR}/F_{\rm rms}$, see Fig. 8). The references listed behind the black hole mass estimates give the origin of the optical spectrum that was used: T13 (*95*), L19 (*32*), F19 (*52*), F20 (*23*), N20 (*57*), C21 (*58*), V21b (this work).

Event	Right Ascension	Declination	90% CL area (deg^2)	Signalness	GCN ref.
IC180908A	$144.58^{+1.45}_{-1.55}$	$-2.13^{+1.20}_{-0.90}$	6.3	0.34	(*96*)
IC181023A	$270.18^{+1.70}_{-2.00}$	$-8.57^{+1.30}_{-1.25}$	9.3	0.28	(*97*)
IC190503A	$120.28^{+0.57}_{-0.77}$	$6.35^{+0.76}_{-0.70}$	1.9	0.36	(*98*)
IC190619A	$343.26^{+4.08}_{-2.63}$	$10.73^{+1.51}_{-2.61}$	27.1	0.55	(*99*)
IC190704A	$161.85^{+2.16}_{-4.33}$	$27.11^{+1.81}_{-1.83}$	21.0	0.49	(*100*)
IC190712A	$76.46^{+5.09}_{-6.83}$	$13.06^{+4.48}_{-3.44}$	92.1	0.30	(*101*)
IC190730A	$225.79^{+1.28}_{-1.43}$	$10.47^{+1.14}_{-0.89}$	5.4	0.67	(*102*)
IC190819A	$148.80^{+2.07}_{-3.24}$	$1.38^{+1.00}_{-0.75}$	9.3	0.29	(*103*)
IC190922A	$167.43^{+3.40}_{-2.63}$	$-22.39^{+2.88}_{-2.89}$	32.2	0.51	(*104*)
IC190922B	$5.76^{+1.19}_{-1.37}$	$-1.57^{+0.93}_{-0.82}$	4.5	0.51	(*105*)
IC191001A	$314.08^{+6.56}_{-2.26}$	$12.94^{+1.50}_{-1.47}$	25.5	0.59	(*106*)
IC191119A	$230.10^{+4.76}_{-6.48}$	$3.17^{+3.36}_{-2.09}$	61.2	0.45	(*107*)
IC191122A	$27.25^{+1.70}_{-2.90}$	$-0.04^{+1.17}_{-1.49}$	12.2	0.33	(*108*)
IC191204A	$79.72^{+3.20}_{-1.74}$	$2.80^{+1.12}_{-1.23}$	11.6	0.33	(*109*)
IC191215A	$285.87^{+2.88}_{-3.19}$	$58.92^{+1.85}_{-2.25}$	12.8	0.47	(*110*)
IC191231A	$46.36^{+4.27}_{-3.47}$	$20.42^{+2.11}_{-2.80}$	35.5	0.46	(*111*)
IC200109A	$164.49^{+4.94}_{-4.19}$	$11.87^{+1.16}_{-1.36}$	22.5	0.77	(*112*)
IC200117A	$116.24^{+0.71}_{-1.24}$	$29.14^{+0.90}_{-0.78}$	2.9	0.38	(*113*)
IC200421A	$87.93^{+3.44}_{-2.83}$	$8.23^{+2.09}_{-1.84}$	24.4	0.33	(*114*)
IC200425A	$100.10^{+4.67}_{-3.14}$	$53.57^{+2.45}_{-1.60}$	19.0	0.48	(*115*)
IC200523A	$338.64^{+10.77}_{-6.07}$	$1.75^{+1.84}_{-3.54}$	90.5	0.25	(*116*)
IC200530A	$255.37^{+2.48}_{-2.56}$	$26.61^{+2.33}_{-3.28}$	25.2	0.59	(*117*)
IC200614A	$33.84^{+4.77}_{-6.39}$	$31.61^{+2.75}_{-2.28}$	47.9	0.42	(*118*)
IC200615A	$142.95^{+1.18}_{-1.45}$	$3.66^{+1.19}_{-1.06}$	5.9	0.83	(*119*)
IC200620A	$162.11^{+0.64}_{-0.95}$	$11.95^{+0.63}_{-0.48}$	1.7	0.32	(*120*)
IC200806A	$157.25^{+1.21}_{-0.89}$	$47.75^{+0.65}_{-0.64}$	1.8	0.40	(*121*)
IC200911A	$51.11^{+4.42}_{-11.01}$	$38.11^{+2.35}_{-1.99}$	52.8	0.41	(*122*)
IC200916A	$109.78^{+1.08}_{-1.44}$	$14.36^{+0.88}_{-0.85}$	4.2	0.32	(*123*)
IC200921A	$195.29^{+2.35}_{-1.73}$	$26.24^{+1.51}_{-1.77}$	12.0	0.41	(*124*)
IC200926A	$96.40^{+0.73}_{-0.55}$	$-4.33^{+0.61}_{-0.76}$	1.7	0.43	(*125*)
IC200926B	$184.75^{+3.64}_{-1.55}$	$32.93^{+1.15}_{-0.91}$	9.0	0.43	(*126*)
IC200929A	$29.53^{+0.53}_{-0.53}$	$3.47^{+0.71}_{-0.35}$	1.1	0.47	(*127*)
IC201007A	$265.17^{+0.52}_{-0.52}$	$5.34^{+0.32}_{-0.23}$	0.6	0.89	(*128*)
IC201014A	$221.22^{+1.00}_{-0.75}$	$14.44^{+0.67}_{-0.46}$	1.9	0.41	(*129*)
IC201021A	$260.82^{+1.73}_{-1.68}$	$14.55^{+1.35}_{-0.74}$	6.9	0.30	(*130*)
IC201115A	$195.12^{+1.27}_{-1.49}$	$1.38^{+1.30}_{-1.11}$	6.6	0.49	(*131*)

Table 3: **IceCube neutrino alerts used in this study.**